Advances in Geo-Energy Research

Vol. 7, No. 3, p. 199-210, 2023

Original article

Three-dimensional simulation of wormhole propagation in fractured-vuggy carbonate rocks during acidization

Piyang Liu[1], Xue Kong[1], Gaocheng Feng[2], Kai Zhang[1,3]*, Shuyu Sun[4], Jun Yao[3]

[1]*School of Civil Engineering, Qingdao University of Technology, Qingdao 266520, P. R. China*

[2]*CNOOC EnerTech-Drilling & Production Co., Tianjin 300452, P. R. China*

[3]*School of Petroleum Engineering, China University of Petroleum (East China), Qingdao 266580, P. R. China*

[4]*Computational Transport Phenomena Laboratory, Division of Physical Sciences and Engineering, King Abdullah University of Science and Technology, Thuwal 23955-6900, Saudi Arabia*

Keywords:
Carbonate rocks
fractures
vugs
acidizing
reactive flow
wormholes

Cited as:
Liu, P., Kong, X., Feng, G., Zhang, K., Sun, S., Yao, J. Three-dimensional simulation of wormhole propagation in fractured-vuggy carbonate rocks during acidization. Advances in Geo-Energy Research, 2023, 7(3): 199-210.
https://doi.org/10.46690/ager.2023.03.06

Abstract:
Acidization is a widely used stimulation technique for carbonate reservoirs aimed at removing formation damage, and if successful, can result in the creation of wormholes of specific lengths and conductivities around the wellbore. The formation of wormholes depends on the injection rate for a particular acid-mineral system and can be predicted through numerical simulations of the reactive phenomenon during acidization. In this paper, the commonly used two-scale continuum model is enhanced to encompass fractured-vuggy porous media. The fractures are characterized by a pseudo-fracture model, while vugs are represented by a cluster of anomalous matrices with high porosity. Moreover, a method for generating random pore-fracture-vuggy models is proposed. The governing equations are discretized by the finite volume method and are solved under three-dimensional linear and radial conditions. Sensitivity analysis of dissolution dynamics with respect to fracture and vug parameters is performed. The simulation results indicate that both fractures and vugs significantly impact wormhole development. Except for fractures perpendicular to the acid flow direction, fractures in other directions play a crucial role in determining the direction of wormhole growth.

1. Introduction

The storage space of the carbonate reservoir is complex due to multi-stage tectonic movement and Karst superposition reconstruction (Liu et al., 2020). In carbonate reservoirs, the coexistence of matrix, fractures, and vugs contributes to the high heterogeneity of the reservoir. Carbonate reservoirs can be classified into three types based on where hydrocarbon is primarily stored and flows through: Pore-type carbonate reservoirs, fractured carbonate reservoirs, and fractured-vuggy carbonate reservoirs (Yao and Huang, 2017). Hydrocarbons are primarily stored in vugs and caves and flow through fractures in fractured-vuggy carbonate reservoirs. Consequently, drilling into large fractured-vuggy bodies is a prevalent method for developing fractured-vuggy carbonate reservoirs (Rafiei and Motie, 2019). However, the exact location of the fractured-vuggy body is challenging to determine due to limitations in seismic resolution. As a result, the well trajectory may not pass through the fractured-vuggy body after drilling is complete, necessitating acid fracturing stimulation to connect the wellbore and the fractured-vuggy body near the wellbore (Aljawad et al., 2019). In contrast, if the well trajectory passes directly through the fractured-vuggy body, mud leakage often occurs due to the large porosity and high permeability of the fractured-vuggy body, reducing the permeability around the wellbore and the oil productivity. In this scenario, acidization is frequently employed to increase the permeability near the wellbore and enhance production rates (Golfier et al., 2002;

Yandy Scientific Press

*Corresponding author.
E-mail address: Piyang.Liu@qut.edu.cn (P. Liu); kongxue6@126.com (X. Kong); fenggch3@cnooc.com.cn (G. Feng); zhangkai@qut.edu.cn (K. Zhang); shuyu.sun@kaust.edu.sa (S. Sun); rcogfr_upc@126.com (J. Yao).

Received January 12, 2023; revised February 1, 2023; accepted February 16, 2023; available online February 20, 2023.

Wang et al., 2020; Alarji et al., 2022).

The principle of acidization stimulation techniques involves injecting acid to dissolve certain rocks in the formation and create high-permeability channels to facilitate the flow of oil and gas (Kalia and Balakotaiah, 2007; Furui et al., 2022). If the injection rate is very high, the chemical reaction rate is very slow compared to the velocity of acid flow. As a result, the injected acid erodes the rock matrix uniformly which may cause some particles to be stripped from the matrix. The eroded particles migrate with injected acid and deposit in some pores or throats. In this case, acidization not only fails to restore the permeability of the damaged region but also leads to new formation damage and consequently reduces the well productivity further. Conversely, if the injection rate is low, the injected acid is completely consumed before penetrating deep into the formation, causing a complete dissolution of rock around the wellbore, reducing borehole stability, and increasing the risk of wellbore collapse (Safari et al., 2017). At an appropriate injection rate, some highly conductive channels known as wormholes are created. Wormholes can pass through the damaged area around the wellbore, thus greatly reducing the resistance of oil and gas flow to the wellbore (Maheshwari and Balakotaiah, 2013; Schwalbert et al., 2019; dos Santos Lucas et al., 2022; Yoo et al., 2022). Therefore, for a given reservoir and acid, the success of the acidizing treatment depends on the ability to find the optimal injection rate at which wormholes are created. Unfortunately, by injecting acid into cores with different sizes, researchers have found that the optimal injection rate is influenced by the core size (Fredd and Fogler, 1999; Seagraves et al., 2018). Therefore, the optimal injection rate obtained from the core acidizing experiments may not valid for field conditions. Alternatively, modeling and simulation of the acidizing process provide an effective option for designing of acidizing treatment (Lohrasb and Junin, 2020).

Numerous models have been developed to characterize the acidization process and predict the conditions under which wormholes form (Hoefner and Fogler, 1988; Daccord et al., 1993; Fredd and Fogler, 1998; Panga et al., 2005; Budek and Szymczak, 2012; Furui et al., 2012; Yoon et al., 2015; Tansey and Balhoff, 2016; Lohrasb and Junin, 2020). The two-scale continuum model developed by Panga et al. (2005) is the most widely adopted and has been further investigated by researchers to examine the impact of formation temperature (Li et al., 2017, 2018; Liu et al., 2019; Aljawad et al., 2021), the type of acid (Ratnakar et al., 2012; Maheshwari et al., 2016; Kiani et al., 2021), flow pattern (Kalia and Balakotaiah, 2007; Ali and Ziauddin, 2020), completion methods (Kalia and Balakotaiah, 2010; Kardooni and Jamshidi, 2022), and medium heterogeneity (Kalia and Balakotaiah, 2009; Huang et al., 2020) on wormhole formation. The two-scale continuum model shows the ability to predict the dissolution patterns observed in experiments and to accurately estimate the breakthrough volume (Panga et al., 2005; Kalia and Balakotaiah, 2007; Liu et al., 2012, 2013; Maheshwari and Balakotaiah, 2013; Jia et al., 2021a). Nevertheless, the reactive flow phenomena that occurred in fractured-vuggy carbonate reservoirs during acidizing cannot be simulated using the two-scale continuum model, because it was developed for pore-type carbonate reservoirs and only accounts for Darcy flow calculations.

Some efforts have been made to investigate the influence of fractures and vugs on dissolution dynamics (Kalia and Balakotaiah, 2009; Izgec et al., 2010; Liu et al., 2017a, 2017b; Huang et al., 2020; Wang et al., 2020; Jia et al., 2021b). Kalia and Balakotaiah (2009) considered fractures and vugs as a matrix with abnormally high porosity and evaluated the role of their location in pattern formation. Their approach comprised of representing each unconnected vug with a block of cells and fracture width with one mesh cell. Liu et al. (2017a) reviewed the literature on reactive flow in fractured carbonate rocks and referred to this representation of fractures as the pseudo-fracture model. By combining the two-scale continuum model with the principle of the discrete fracture model, Liu et al. (2017b) developed a new model, which is effective for a systematic investigation of the reactive flow phenomenon in fractured carbonate rocks. They numerically solved the model using the finite-volume method and performed a sensitivity analysis of the dissolution process with respect to fracture parameters. Subsequently, Chen et al. (2018) and Khoei et al. (2020) solved the reactive flow model of fractured medium using the unified pipe-network method and the extended finite element method, respectively. Although the model developed by Liu et al. (2017b) can account for the effect of each individual fracture on wormhole propagation, there is still a challenge in simulating this model in three-dimensional (3-D) cases, associated with the mesh discretization of the domain. In order to accurately capture the complexity of fracture geometry, an unstructured discretization scheme is required. Unstructured discretization of the 3-D domain containing fractures is complex and cumbersome, especially when the distance or included angle between adjacent fractures is small, a tiny mesh is needed to represent the region between two fractures. In the numerical simulation, the time step is limited by the smallest mesh. Therefore, a low-quality mesh can result in numerical instability. Huang et al. (2020) and Qi et al. (2019) viewed vugs as anomalous matrices with high porosity and solved the reaction flow model using COMSOL software, exploring the effect of the presence of vugs on wormhole structure. Wang et al. (2020) treated fractures and vugs as matrices with abnormal porosity and used the sequential Gaussian simulation algorithm in GSLIB software to generate vugs resembling actual shapes. It is worth noting that all these numerical simulations of reactive flow in fractured-vuggy carbonate reservoirs were performed in a two-dimensional (2-D) domain. To the best of the authors' knowledge, no study has been conducted on the simulation of reactive flow in fractured-vuggy carbonates in a 3-D domain. However, wormhole formation in fractured-vuggy carbonate rocks is a complex 3-D phenomenon. In addition, numerical simulation results of reactive flow in pore-type media by Maheshwari and Balakotaiah (2013) showed that 2-D simulation results can reflect the qualitative features of the dissolution structure, but are inexactitude quantitatively. Therefore, 3-D numerical simulations are required to study the dissolution process under actual conditions and obtain complete information about the

impact of the presence of fractures and vugs on wormhole propagation.

The aim of this work is to enhance the two-scale continuum model to encompass fractured-vuggy porous media and to solve the model under 3-D conditions to assess the impact of the characteristic parameters of fractures and vugs on the dissolution dynamics during acidizing. The pseudo-fracture model is utilized to represent fractures and vugs are depicted as clusters of anomalous matrices with high porosity. In particular, the matrix, fractures, and vugs are discretized with the same grid system. An approach for generating initial random porosity, random fractures, and random vugs is established. The Stokes-Brinkman equation is employed to uniformly describe fluid flow in the matrix, fractures, and vugs, instead of the Darcy equation used in the two-scale continuum model.

The paper is structured as follows: Section 2 briefly introduces the two-scale continuum model, which was developed previously for pore-type carbonate reservoirs, and extends it to describe the reactive transport of acid in the fractured-vuggy porous medium. In Section 3, the boundary and initial conditions are specified. Particularly, the approach for generating the initial pore-fracture-vug model is explained. Section 4 derives the dimensionless form of the extended model. Section 5 briefly outlines the numerical algorithm for solving the presented model. In Section 6, 3-D numerical experiments are conducted under linear and radial flow conditions to examine the influence of characteristic parameters of fractures and vugs on the acidization process. The main results of this work are summarized in the last section.

2. Mathematical model

The fluid flow in the fractured-vuggy medium encompasses both the porous flow within the porous matrix and the free flow in vugs. Currently, two main approaches exist for solving this coupled problem: single-domain and two-domain approaches. (Yao and Huang, 2017). The single-domain approach considers the entire coupling flow region as a continuous system through the introduction of the concept of an interface transition region. This allows for the description of fluid flow in the entire region through a unified set of flow equations. On the other hand, the two-domain approach establishes separate governing equations for fluid flow in two different flow regions and then couples these two models through specific interface conditions. In the context of acidization, the transported acid reacts with the rock, leading to continuous changes in the geometry of the vug. Because it is challenging to couple porous flow and free flow at an interface that is continually changing, the single-domain approach is utilized to describe the flow of injected acid in fractured-vuggy carbonate rocks. The unified flow equation is expressed using the Stokes-Brinkman equation as follows (Yuan et al., 2019):

$$\mu \mathbf{K}^{-1}\mathbf{v} + \nabla P - \mu_e \nabla^2 \mathbf{v} = 0 \tag{1}$$

$$\frac{\partial \phi}{\partial t} + \nabla \cdot \mathbf{v} = 0 \tag{2}$$

where P denotes the pressure; μ and $\mathbf{v}$ are the viscosity and velocity of the fluid, respectively; ϕ and $\mathbf{K}$ are the porosity and permeability tensor of the porous medium, respectively; t is the time. μ_e is the effective viscosity and dependent on the structural characteristics of porous media and serves to match the shear stress at the interface between the free flow region and the porous media region. In most applications, it takes the same value as the fluid viscosity. In Eqs. (1) and (2), the effect of compressibility on the pore volume, induced by both the fluid and rock, is neglected due to the greater impact of reactive dissolution on porosity.

The material balance equation for the acid solute in the liquid phase is:

$$\frac{\partial(\phi C)}{\partial t} + \nabla \cdot (\mathbf{v}C) = \nabla \cdot (\phi \mathbf{D}_\mathrm{e} \cdot \nabla C) - \frac{k_s k_c a_v}{k_s + k_c} C \tag{3}$$

where C is the concentration of acid in the liquid phase; $\mathbf{D}_\mathrm{e}$ is the effective dispersion tensor; k_c is the mass transfer coefficient; k_s is the surface reaction rate; a_v is the specific surface area. It should be noted that in Eq. (3) the $HCl-CaCO_3$ reaction is assumed as an irreversible first order reaction.

The chemical reaction leads to the dissolution of the rock, and the change of porosity is expressed as:

$$\frac{\partial \phi}{\partial t} = \frac{k_s k_c a_v \alpha}{(k_s + k_c)\rho} C \tag{4}$$

where ρ is the rock density; α indicates the dissolving power of the acid, and it is defined as grams of dissolved solid per mole of consumed acid.

In order to effectively solve the aforementioned equations, it is imperative to determine the values of the permeability K, dispersion tensor $\mathbf{D}_\mathrm{e}$, mass transfer coefficient k_c, and specific surface area a_v. These values are contingent upon the pore structure and exhibit continuous variations in response to the chemical reaction. Their values can be calculated as follows (Panga et al., 2005):

$$\frac{K}{K_0} = \frac{\phi}{\phi_0}\left[\frac{\phi(1-\phi_0)}{\phi_0(1-\phi)}\right]^2 \tag{5}$$

$$\frac{r_p}{r_0} = \sqrt{\frac{K}{K_0}\frac{\phi}{\phi_0}} \tag{6}$$

$$\frac{a_v}{a_0} = \frac{\phi}{\phi_0}\frac{r_0}{r_p} \tag{7}$$

where ϕ_0, K_0, r_0, a_0 are the initial average porosity, initial average permeability, initial average pore radius, and initial specific surface area, respectively; r_p is the pore radius.

Both the mass transfer coefficient and the diffusion coefficient of the acid solute are related to the acid rock reaction, and they are expressed by the following relations:

$$\mathrm{Sh} = \frac{2k_c r_p}{D_m} = \mathrm{Sh}_\infty + 0.7\sqrt{\mathrm{Re}}\sqrt[3]{S_c} \tag{8}$$

$$D_{eX} = \alpha_{os} D_m + \lambda_X \frac{2|\mathbf{v}|\, r_p}{\phi} \tag{9}$$

$$D_{eT} = \alpha_{os} D_m + \lambda_T \frac{2|\mathbf{v}|\, r_p}{\phi} \tag{10}$$

where Sh is the Sherwood number; D_m is the molecular diffusion coefficient; Sh_∞ is the asymptotic Sherwood number; Re is the pore Reynolds number, defined as $\mathrm{Re} = 2r_p|\mathbf{v}|/\nu$, where ν is the kinetic viscosity; S_c is the Schmidt number,

defined as $S_c = \nu/D_m$. The subscripts X and T denote the direction of acid injection and the direction perpendicular to it, respectively. α_{os}, λ_X and λ_T are constants related to the pore structure.

3. Boundary and initial conditions

3.1 Boundary condition

The boundary conditions at the inlet are:

$$v_{in} = v_0 \tag{11}$$

$$v_0 C_0 = v_0 C - \phi D_{eX} \frac{\partial C}{\partial \vec{n}} \tag{12}$$

where v_{in} is the component of fluid velocity along the injection direction, v_0 is the injection velocity, $\vec{n}$ is the unit vector in the direction of fluid flow and C_0 is the injected acid concentration.

Constant pressure boundary conditions are used at the outlet and the flow is assumed to be a fully developed flow. The pressure P, velocity $\mathbf{v}$, and concentration C at the outlet satisfy the following equations:

$$P = P_e, \quad \frac{\partial \mathbf{v}}{\partial \vec{n}} = 0, \quad \frac{\partial C}{\partial \vec{n}} = 0 \tag{13}$$

where P_e denotes the outer boundary pressure and its value is a constant.

For the other boundaries, the no-slip boundary condition is used:

$$\mathbf{v} = 0, \quad \frac{\partial C}{\partial \vec{n}} = 0 \tag{14}$$

3.2 Initial condition

The initial conditions of the acid concentration is expressed as:

$$C|_{t=0} = 0 \tag{15}$$

The distribution of the initial porosity, fracture, and vug plays a significant role in wormhole formation. Considerable efforts have been devoted to generating an appropriate initial porosity field. The method presented by Liu et al. (2019) is adopted here, which is described in Algorithm 1.

The initial distribution of fractures is obtained by generating a random discrete fracture network. In 2-D domains, fractures are represented as lines and in 3-D domains, they are represented as planes. Each fracture is characterized by its central location, orientation, length, and aperture. The fracture network can be generated through the Algorithm 2.

The Liang-Barsky algorithm (Liang and Barsky, 1984) is utilized to clip fractures when the edge of the clipping window is a straight line, which pertains to the linear flow scenario addressed in this work. However, in cases of radial flow where the shape of the inner and outer boundaries of the physical domain is circular, the Liang-Barsky algorithm is no longer applicable. Hence, an efficient algorithm is developed to clip lines outside a circular window. The procedure of this algorithm is described in Algorithm 3.

In the numerical simulation, the generated discrete fracture

Algorithm 1: Porosity field generation algorithm

Input: average permeability, average porosity, number of grids in x, y, and z directions, correlation length, heterogeneity magnitude of the permeability field

Output: The porosity field with specified correlation length and heterogeneity

1 Generate random numbers that are normally distributed with zero mean and unit variance.
2 Compute the kernel matrix using the square root of the Gaussian covariance model.
3 Compute the correlated Gaussian distribution by convolving the numbers generated in Step 1 with the kernel matrix calculated in Step 2.
4 Compute the mean and standard deviation of the permeability using the input heterogeneity magnitude.
5 Add the mean to the correlated Gaussian distribution calculated in Step 3.
6 Compute the exponential of the sum calculated in Step 5 to obtain a log-normally distributed permeability field.
7 Solve Eq. (5) to get the porosity field with specified correlation length and heterogeneity.

Algorithm 2: Fracture network generation algorithm

Input: domain size, number of fractures, the mean value and standard deviation of the azimuth of fractures, correlation length, the rate parameter of the negative exponential distribution for characterizing fracture trace

Output: The starting and ending coordinates of each fracture in fracture networks

```
Generate fracture central coordinates from uniform distribution
Generate fracture orientation from normal distribution
Generate fracture length from negative exponential distribution
while the counter is less than or equal to the number of fractures do
    compute the coordinates of the start and end point of the fracture
    if the fracture starts or ends outside the physical domain then
        clip the portion of the fracture outside the physical domain
        compute the coordinates of the start and end point of the clipped fracture
    end
end
```

Algorithm 3: Line clipping algorithm for circular window

Input: center coordinates and radius of the circular window, the starting and ending coordinates of line segments to be clipped

Output: Coordinates of the start and end points of the clipped segment

Compute the distance (d_ij) between the endpoint (p_ij) of the line segment and the center (c_0) of the circular window. `// The subscript ij refers to the j-th endpoint of the i-th line segment`
Generate fracture orientation from normal distribution
Generate fracture length from negative exponential distribution
for *i = 1 to the number of line segments* **do**
  if *d_i1 < r_0 and d_i2 < r_0* `// r_0 is the radius of the circular window`
  then
    print the original endpoint coordinates of the i-th segment
  end
  else if *d_i1 > r_0 and d_i2 < r_0* **then**
    compute the intersection coordinates of the i-th segment and circle
    print the intersection coordinates and the 2nd endpoint coordinates
  end
  else if *d_i1 > r_0 and d_i2 < r_0* **then**
    compute the intersection coordinates of the i-th segment and circle
    print the intersection coordinates and the 1st endpoint coordinates
  end
  else if *d_i1 > r_0 and d_i2 > r_0* **then**
    if *d_i1 >= d_i2* **then**
      compute two tangents to the circle pass through the 1st endpoint of the i-th segment
      if *the 2nd point of the i-th line segment is on the opposite side of the two tangents* **then**
        compute the coordinates of two intersections of line segment and circle
        print the coordinates of two intersections of line segment and circle
      end
      else
        eliminate the i-th line segment
      end
    end
    else
      exchange the two endpoints of the i-th line segment
      repeat Steps 19 to 26
    end
  end
end

network is represented using the pseudo-fracture model. The critical task is to identify the fracture grids, which is accomplished by checking whether the edge of each grid intersects with a fracture. If the edge of a grid cell intersects with any fracture, the two adjacent grids straddling the edge are then marked as fracture grids.

After identifying the index numbers of grids that the fractures traverse, the fractures can be represented by assigning high porosity values to these grids. The porosity value assigned to the fracture grids can be determined through the cubic law, where the fracture permeability, K_f, can be calculated as $K_f = b^2/12$, based on the fracture aperture, b. In this work, the fracture aperture is set to 1 mm, resulting in a calculated fracture permeability of 8×10^7 md. The average porosity of the matrix is assumed to be 0.35 and its average permeability is assumed to be 100 md. The porosity of the fracture grids is calculated to be 0.99 using Eq. (5), and this value is used in the numerical experiments. It should be noted that the algorithm for generating the initial fracture field, as described above, is only applicable for the 2-D case. In the 3-D domain, the line segments representing the fractures are extended into planes along the vertical direction.

In the generation of random vugs, a porosity field characterized by a large correlation length and pronounced heterogeneity is first generated. Then, areas with porosity greater than the average porosity are designated as vug units. The remaining work is to identify the grid index numbers of these vug units and modify the corresponding porosity values. The porosity in the vug area may vary between the average matrix porosity and 1, reflecting different levels of filling within the vug. In this study, the porosity of the vuggy unit is set as 0.9.

4. Dimensionless model

Define the following dimensionless parameters:

$$x_D=\frac{x}{L}, y_D=\frac{y}{L}, z_D=\frac{z}{L}, r_D=\frac{r}{L}, r_{wD}=\frac{r_w}{L}, \mathbf{U}=\frac{\mathbf{v}}{v_0}$$
$$t_D=\frac{tv_0}{L}, r_{pD}=\frac{r_p}{r_0}, a_{vD}=\frac{a_v}{a_0}, \chi=\frac{L^2}{K_0}, \kappa=\frac{\mathbf{K}}{K_0}=\frac{\mathbf{K}}{L^2}\chi$$
$$\mathbf{D}=\frac{\mathbf{D}_e}{D_m}, C_D=\frac{C}{C_0}, P_D=\frac{(P-P_e)K_0}{\mu v_0 L}, h_T^2=\frac{2k_s r_0}{D_m}$$
$$Da=\frac{k_s a_0 L}{v_0}, N_{ac}=\frac{\alpha C_0}{\rho}, \eta=\frac{2r_0}{L}$$

where the subscript D denotes dimensionless; L denotes the characteristic length in the flow direction, which is taken as the core length in the linear condition and the radius of the core in the radial condition; r is the coordinate variable in the cylindrical coordinate; r_w is the radius of the injection well; $\mathbf{U}$ is the dimensionless velocity vector; κ is the dimensionless permeability; K_0, r_0 and a_0 denote the initial permeability, average pore radius, and initial specific surface area, respectively. η and χ are the proportionality coefficients.

After defining the dimensionless parameters, a new set of parameters are obtained as Thiele modulus h_T^2, Damköhler number D_a and acidification capacity constant N_{ac}. Thiele modulus h_T^2 is defined as the ratio of the reaction rate to the diffusion rate at the initial pore volume. Damköhler number D_a is defined as the ratio of reaction velocity to convection velocity at the core scale. The acidizing capacity constant N_{ac} is defined as the volume of solid dissolved per unit volume of acid.

The Eqs. (1)-(4) can be written in the following dimensionless form:

$$\kappa^{-1}\mathbf{U}+\nabla P_D-\chi^{-1}\nabla^2\mathbf{U}=0 \tag{16}$$
$$\frac{\partial\phi}{\partial t_D}+\nabla\cdot\mathbf{U}=0 \tag{17}$$
$$\frac{\partial(\phi C_D)}{\partial t_D}+\nabla\cdot(\mathbf{U}C_D)=\nabla\cdot(\mathbf{D}\cdot\nabla C_D)-\frac{\mathrm{Sh}D_a a_{vD}C_D}{\mathrm{Sh}+h_T^2 r_{pD}} \tag{18}$$
$$\frac{\partial\phi}{\partial t_D}=\frac{\mathrm{Sh}D_a N_{ac}a_{vD}C_D}{\mathrm{Sh}+h_T^2 r_{pD}} \tag{19}$$

5. Numerical method

The above Eqs. (16)-(19) are decoupled by utilizing the sequential solution method. The method starts by solving the Stokes-Brinkman equation to obtain the pressure and velocity fields. The calculated velocity field is then substituted into the solute transport equation and combined with the reaction equation, enabling the calculation of the concentration of the injected acid and porosity at the subsequent time step.

The equations are discretized using the finite volume method. As a result, the discretized Stokes-Brinkman equation can be expressed as a linear system of equations:

$$\begin{bmatrix}\mathbf{F} & \mathbf{B}^{\mathrm{T}}\\ \mathbf{B} & \mathbf{0}\end{bmatrix}\begin{bmatrix}\mathbf{v}\\ \mathbf{P}\end{bmatrix}=\begin{bmatrix}\mathbf{f}_b\\ \mathbf{f}_\phi\end{bmatrix} \tag{20}$$

The presence of a zero diagonal block in the coefficient matrix of Eq. (20), which is characteristic of saddle point problems, suggests that the velocity and pressure cannot be found simultaneously using the above equation. It can be seen from Eq. (16) that the pressure is in the form of a gradient in the momentum equation. In other words, an explicit equation for computing the pressure field is unavailable, so the pressure correction equation needs to be supplemented. This is accomplished by adopting the Semi Implicit Method for Pressure Linked Equations (SIMPLE) algorithm. To overcome the issue of uncoupling between the pressure and velocity fields and to solve the model in both Cartesian grids (for linear flow cases) and non-Cartesian grids (for radial flow cases) with the same procedure, the current work employs the collocated grid in conjunction with the Rhie-Chow interpolation technology. This means that both the pressure and velocity variables are stored at cell centroids.

The operator splitting method is adopted to decouple the reactive-transport process. In any single time step, Eq. (21) is solved first to obtain the acid concentration field at t^*, indicating the time when the transport of the acid solute has been completed but the chemical reaction has not yet occurred:

$$\begin{cases}\dfrac{\partial(\phi C_D)}{\partial t_D}+\nabla\cdot(\mathbf{U}C_D)=\nabla\cdot(\mathbf{D}\cdot\nabla C_D)\\ \dfrac{\partial\phi}{\partial t_D}=0\end{cases} \tag{21}$$

Subsequently, Eq. (22) is solved to incorporate the effect of chemical reactions:

$$\begin{cases}\dfrac{\partial}{\partial t_D}\left(\phi C_D+\dfrac{\phi}{N_{ac}}\right)=0\\ \dfrac{\partial\phi}{\partial t_D}=\dfrac{\mathrm{Sh}D_a N_{ac}a_{vD}C_D}{\mathrm{Sh}+h_T^2 r_{pD}}\end{cases} \tag{22}$$

6. Results and analysis

In this section, the influence of fracture and vug characteristic parameters on the acidizing process is analyzed through 3-D numerical experiments under linear and radial flow conditions. The parameters utilized in the simulations are listed in Table 1 and remained constant throughout the study, unless otherwise specified. It should be mentioned that the injection velocity of acid used in simulations is determined through numerical experimentation. This injection velocity is selected such that wormholes would be formed. The injection velocities used in the numerical simulations of linear and radial flow conditions are 0.002 and 0.005 cm/s, respectively. In Table 1, r_e is the radius of the core used in radial flow simulations. V_{DP} is the Dykstra-Parsons coefficient (Liu et al., 2019), which is commonly used in the petroleum industry to quantify the permeability variation and can be related with the stand deviation of $\ln(K)$, i. e., σ as:

$$V_{DP}=1-e^{-\sigma} \tag{23}$$

6.1 Effect of fracture parameters on wormhole propagation

6.1.1 Fracture density

In this subsection, the impact of fracture density on the formation of wormholes is investigated through numerical simulation experiments. The number of fractures, N_f, ranges

Table 1. List of values of parameters used in the simulation.

Parameters	Values	Parameters	Values
L	10 cm	Sh_∞	3
H	4 cm	N_{ac}	0.1
W	4 cm	S_c	1000
r_e	10 cm	η	10^{-6}
ϕ_0	0.35	χ	10^9
K_0	100 md	α_{os}	0.5
V_{DP}	0.75	λ_X	0.5
h_T^2	0.07	λ_T	1

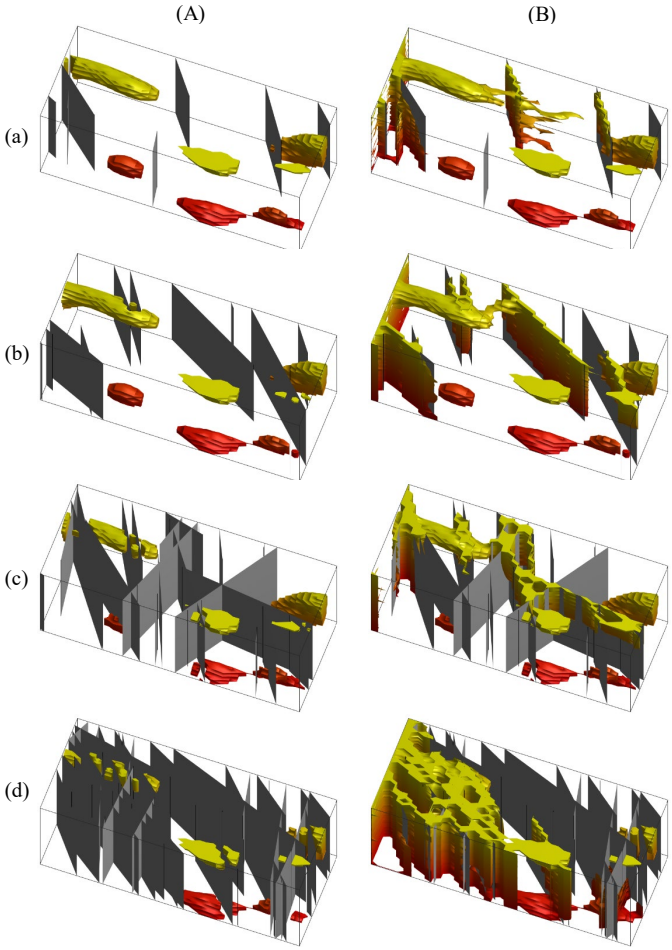

Fig. 1. Dissolution structures for different number of fractures: (a) $N_f = 7$, (b) $N_f = 10$, (c) $N_f = 20$, (d) $N_f = 30$. Column (A) indicates the initial distribution of fractures and vugs and column (B) shows the dissolution structures when acid breakthrough.

from 7 to 30, while the orientation and length of the fractures are fixed. Fractures are with a mean orientation of 60° and a standard deviation of 50°. The average length of the fractures is $L/2$. Because fractures are randomly generated, the fracture length and orientation are somewhat different when changing the number of fractures. Fig. 1, column (A) illustrates the superposition of the different fracture distributions on the fixed vug distribution.

Fig. 1, column (B) presents a comparison of the wormhole structures for cores with varying numbers of fractures. When the number of fractures is low (Fig. 1, row (a)), wormholes primarily develop along vugs and, upon completion of the dissolution process, a majority of the vugs become integrated into the wormhole. This suggests that vugs exert a controlling influence over the wormhole's growth direction when the number of fractures is small. As the number of fractures increases (Fig. 1, row (b) and (c)), the connectivity between fractures increases and the role of vugs in wormhole propagation decreases. As a result, the injected acid mainly flows along the fractures. In cases where the number of fractures is high (Fig. 1, row (d)), the influence of vugs on wormhole propagation is virtually negligible. The acid flows almost exclusively along the fractures, which become part of the wormhole and emerge as the controlling factor in wormhole propagation.

Additionally, when the number of fractures is low (Fig. 1, row (a) and (b)), nearly every fracture is affected by the injected acid. However, as the number of fractures increases (Fig. 1, row (c) and (d)), only some fractures become part of the wormhole upon completion of the dissolution process and some remain untouched by the acid when it breaks through the core. This is due to competition between fractures as the number of fractures increases.

Fig. 2 displays the breakthrough volume (PV_{BT}) of cores with varying numbers of fractures as depicted in Fig. 1. The breakthrough volume is defined as the ratio of the cumulative volume of the injected acid to the initial pore volume of the core when the acid penetrates the core. As illustrated, the breakthrough volume decreases with the increase in the number of fractures. However, contrary to our intuitive expectation, the breakthrough volume does not exhibit a continuous decline with the increase of the number of fractures, as the core with 30 fractures demonstrated a larger breakthrough volume compared to the core with 20 fractures. In combination with Fig. 1, it can be inferred that the breakthrough volume does not exhibit a direct correlation with the number of fractures. The reduction in breakthrough volume is due to the increased connectivity between fractures as the number of fractures increases. Because the resistance for fluid flow of fractures is small, the injected acid tends to flow along the fractures. As a result, only a small part of the rock is dissolved to break through the core. However, if the increased number of fractures does not play a connecting role, the injected acid still needs to dissolve the matrix to form a through wormhole. In this case, some of the injected acid will filter along the fracture wall during the growth of the wormhole, leading to increased acid consumption. As evidenced in row (d) of Fig. 1, although the number of fractures is large, only fractures on the left or right are connected but not those between the left and right. The acid injection into fractures on the left half initiates the dissolution of matrix and extends the wormhole forward. At the same time, the fracture wall undergoes dissolution, causing an increase in fracture aperture and ultimately leading to the significant dissolution of matrix and greater consumption of injected acid.

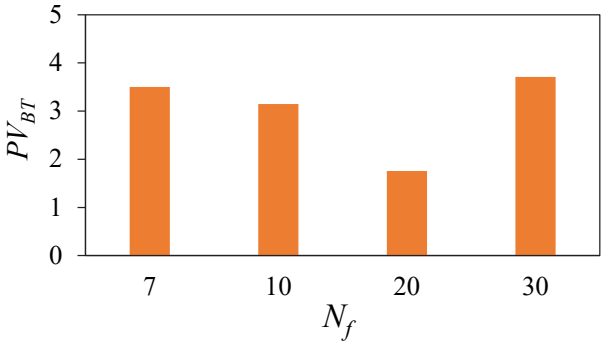

Fig. 2. Comparison of breakthrough volume for cores with various fracture numbers.

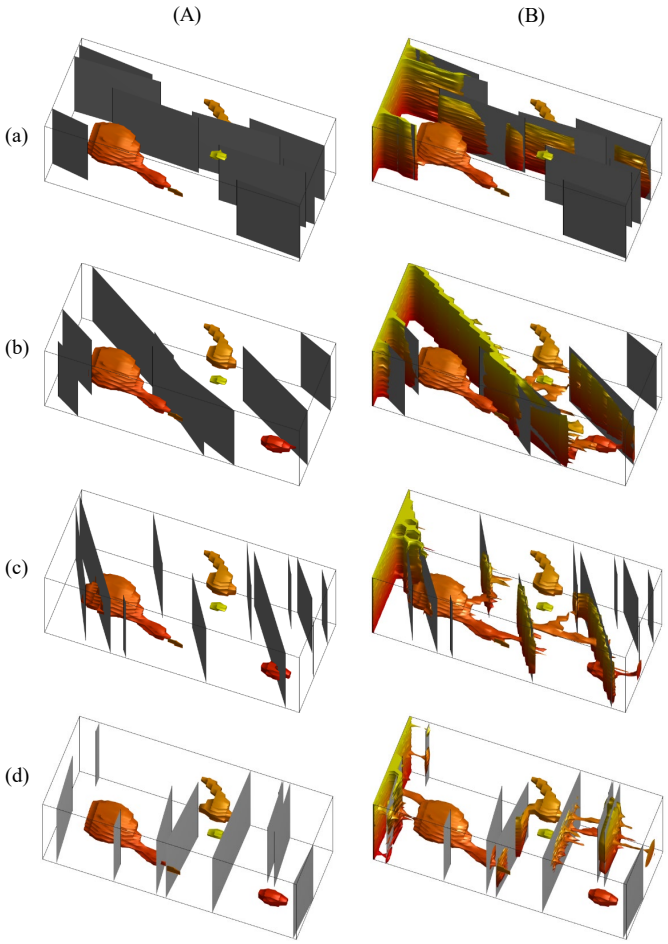

Fig. 3. The distribution of fractures and vugs (A) and wormhole structures (B) for different fracture orientations (a) $\theta_f = 0°$, (b) $\theta_f = 30°$, (c) $\theta_f = 60°$, (d) $\theta_f = 90°$.

6.1.2 Fracture orientation

The impact of altering fracture orientation on the wormhole structure is examined in this subsection. The fracture orientation, defined as the angle between the fracture direction and the core axis, is represented by θ_f. The mean values of fracture orientation are 0°, 30°, 60°, and 90°, with a standard deviation of 5°, when fractures are generated randomly. Fractures with an average length of $L/3$ and a quantity of 10, overlaid a fixed vug distribution as depicted in Fig. 3, column (A). The wormhole structures for the corresponding fracture distributions are shown in Fig. 3 column (B).

Inspection of Fig. 3 reveals that when the angle between the fracture and the flow direction is small, the fracture integrates into the wormhole structure and allows for breakthrough with limited rock dissolution. The variance in fracture orientation resulted in divergent wormhole structures after acid breakthrough. For instance, when the angle between the fracture and the injected acid flow is less than 45°, such as in Fig. 3, row (b) with an orientation of 30°, the wormhole predominantly grew along the fracture, eventually leading to a wormhole direction that coincided with the fracture orientation. Conversely, when the angle exceeded 45°, as in the case of an orientation of 60° in Fig. 3, row (c), while some fractures remained part of the wormhole, its direction is no longer aligned with the fracture orientation, and fractures are unable to dictate wormhole growth direction. In the extreme scenario, where the orientation is 0° (Fig. 3, row (a)), the wormhole entirely developed along the fractures, indicating that fractures played a crucial role in determining the wormhole's growth direction. If the fracture orientation is perpendicular to the fluid flow direction, as depicted in Fig. 3, row (d), the wormhole growth will not connected to the fracture orientation, but proceed forward along the matrix with the least permeability resistance, beyond the vertical fracture. Although the vertical fracture does not control the wormhole growth direction, it influences its path.

It can also be seen from Fig. 3 that after the acid enters the fracture, not the whole surfaces of the fracture can be dissolved. Instead, the acid selectively dissolves only parts of the fracture surface (as shown in Fig. 3, row (d)). This effect cannot be replicated in 2-D numerical simulations. Furthermore, the resulting wormhole exhibits more branching when the fractures are oriented at 30°, 60°, and 90° (as demonstrated in Fig. 3, row (b), row (c), and row (d)). Conversely, when the fractures are oriented at 0°, in the same direction as the injected acid flow (Fig. 3, row (a)), the generated wormhole presents almost no obvious branching.

In Fig. 4, the calculated breakthrough volume is plotted against fracture orientation. As indicated in Fig. 4, as fracture orientation increases up to 90°, the breakthrough volume also increases. This result is due to an increase in branching of the wormholes, which occurs as the fractures shift from being aligned with the flow direction of the injected acid to a direction perpendicular to the flow direction. The increased branching of the wormholes indicates a greater degree of rock erosion, thus requiring a larger volume of acid.

6.1.3 Fracture length

In this subsection, the influence of fracture length on wormhole propagation is analyzed. Numerical simulations are performed on cores containing fractures with an average length of $L/5$, $L/4$, $L/3$, and $L/2$. The mean value of the fracture orientation is 60° with a standard deviation of 50°. The number of fractures is 15. The fracture distribution and the corresponding simulation results are depicted in Fig. 5.

When the injected acid breaks through the core, the varying

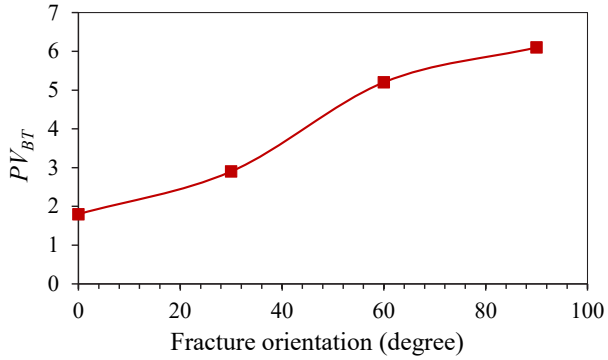

Fig. 4. The effect of fracture orientation on PV_{BT} corresponds to the dissolution structures in Fig. 3 column (B).

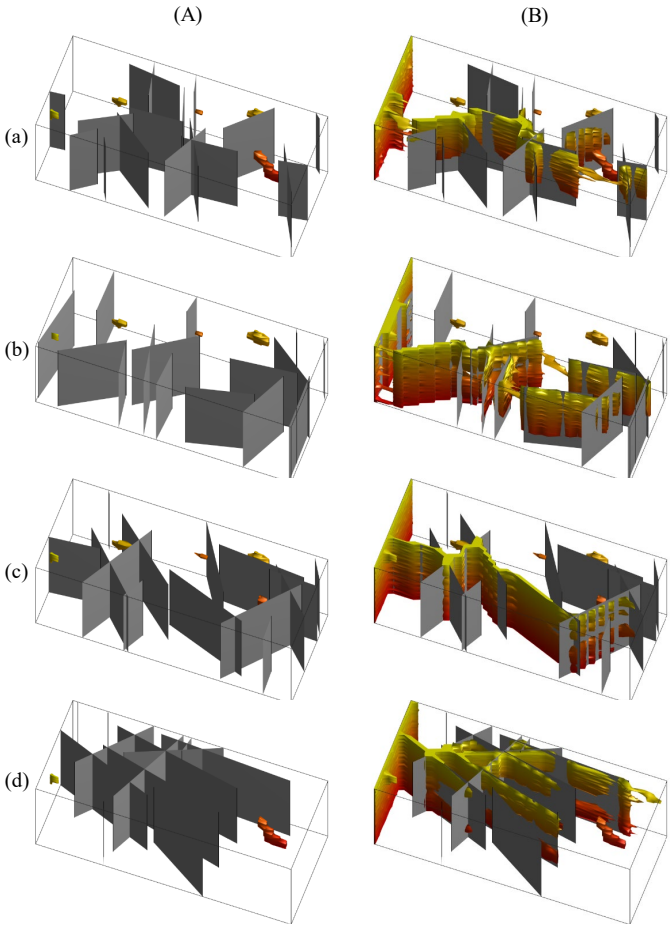

Fig. 5. Comparison of wormhole structures for average fracture length of (a) $L/5$, (b) $L/4$, (c) $L/3$, (d) $L/2$. Column (A) indicates the initial distribution of fractures and vugs and column (B) shows the dissolution structures when acid breakthrough.

fracture lengths result in a distinct wormhole structure. For example, when the fractures are relatively short (Fig. 5 row (a) and row (b)), the resulting wormholes are broad and branched with an irregular growth pattern. As the fracture length increases (Fig. 5 row (c) and row (d)), the fractures can be connected, allowing the injected acid to pass through the fractures faster and preventing the formation of ramified

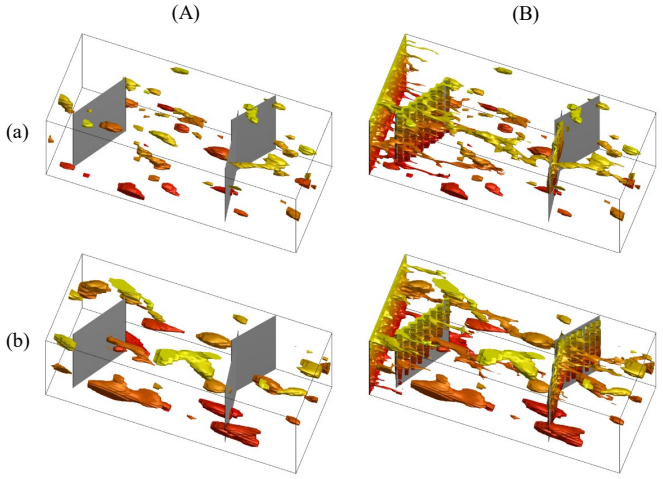

Fig. 6. The vug distributions (A) and wormhole structures (B) for (a) $l_x = 0.1$, $l_y = 0.05$, $l_z = 0.05$; (b) $l_x = 0.2$, $l_y = 0.1$ $l_z = 0.1$.

wormholes. As a result, the area of dissolution is reduced, the wormhole produces fewer branches, and the wormhole is more regular. The direction of the wormhole follows exactly the orientation of the fracture.

As the fracture length increases (Fig. 5, column (B)), the influence of fracture length on wormhole direction becomes more pronounced and the number of branched wormholes decreases. The generated wormhole ultimately aligns with the orientation of the fracture, with the fracture becoming part of the wormhole.

6.2 Effect of vug size on wormhole propagation

This subsection studies the effect of vug size on wormhole propagation. As discussed in Section 3.2, the vug size is determined by the correlation length. As the correlation length increases in each direction, the size of the generated vugs also increases, as demonstrated in Fig. 6, column (A). The corresponding wormhole structures are shown in Fig. 6 column (B).

It is evident from column (B) of Fig. 6 that, irrespective of vug size, the resultant wormhole only permeates a portion of the vugs and a majority of the vugs remain unscathed by the injected acid. Instead, the fractures extend as the wormhole grows and become part of the wormhole. Therefore, the fractures exert a stronger influence on the growth direction of the wormhole than the vugs. This is due to the fractures serving as a highly permeable pathway for the flow of injected acid, extending over a greater length than the vugs.

As can be seen from the results in row (b) of Fig. 6, the injected acid does not preferentially enter the larger volume of the vug. When the injected acid breaks through the core, there are still voluminous vugs that are untouched by the injected acid. This is because the vugs are connected to each other through the matrix. The injected acid flows preferentially into the channel with the least permeability resistance and increases the permeability of this channel, inhibiting acid flow to other areas.

Table 2. Parameters and values used for generating the initial fracture and vug distributions.

Case	N_f	Average fracture length	Fracture azimuth (°)		V_{DP} of vug	Correlation length of vug
			Mean value	Standard deviation		
(A)	10	$2r_e/3$	30	5	0.9	0.05
(B)	15	$2r_e/3$	60	5	0.85	0.1
(C)	20	$r_e/3$	60	30	0.85	0.1

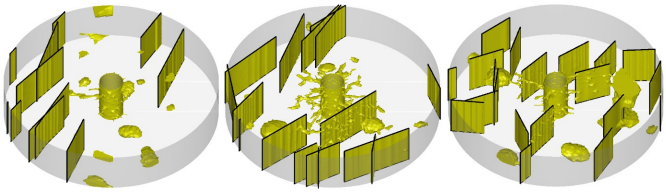

Fig. 7. Fractured-vuggy distributions and wormhole structures corresponding to Cases (A), (B) and (C) in Table 2.

6.3 Radial flow cases

In practical reservoir acidizing treatments, the flow state of acid is radial in nature. Thus, simulation analysis of acidizing under radial flow conditions is necessary. In this subsection, three simulation cases, labeled as Case (A), Case (B), and Case (C), are carried out. The parameter values used to generate the porosity field are taken from Table 1, while the values used to generate the initial fracture and vug distributions are listed in Table 2. The wormhole structures corresponding to each case are depicted in Fig. 7.

When comparing cases (A) and (B) where the number of fractures is 10 and 15 respectively, as shown in Fig. 7, it becomes apparent that the control effect of the wormholes by fractures does not significantly vary with an increase in the number of fractures. This result is in stark contrast to that observed under linear flow conditions. This is because that, under radial flow, fractures provide a highly permeable channel for acid flow, regardless of their location, and only the fracture with the least resistance to flow works.

As we move to cases (B) and (C) where the average length of fractures are $2r_e/3$ and $r_e/3$ respectively, Fig. 7 highlights that the wormholes are more branched when the fractures are relatively short. As the fracture length increases, the fractures become interconnected, allowing the injected acid to traverse the fractures more efficiently and resulting in fewer branches in the formed wormhole.

A comparison of the fracture orientation in Cases (A), (B), and (C) reveals that in the simulation of acid dissolution wormholes under radial flow conditions, the effect of the fracture orientation is no longer the same as that under linear flow conditions. Under linear flow, fractures oriented at less than 45° play a dominant role in dictating the orientation of the wormhole. In contrast, under radial flow conditions, the role fractures play in determining the direction of the wormhole is contingent upon whether they are distributed along the radial direction of fluid flow. If the fractures are not aligned with the radial direction, their orientation has no influence on the direction of the wormhole.

7. Conclusions

The present study endeavors to accomplish the numerical simulation of wormhole propagation under 3-D linear and radial conditions. By analyzing the effect of the characteristic parameters of fracture and vug on the dissolution dynamics, the following results are summarized:

1) Both fractures and vugs are dominant factors in the propagation of wormholes. In comparison to vugs, fractures exhibit a more pronounced effect on wormhole propagation.
2) The propagation of wormholes is affected by the orientation of fractures. When the angle between the pathway formed by fractures and the flow direction is less than 45°, the propagation of wormholes is primarily dominated by the presence of fractures. When the orientation of the fracture is perpendicular to the flow direction, fractures have a limited effect on the propagation of the primary wormhole, but they may influence the direction and extent of wormhole branching.
3) When the number of fractures is small, the vug plays a controlling role in the growth direction of the wormhole. Fractures can provide highly permeable channels for injected acid flow and have long lengths compared to vugs. These advantages make it possible that when fractures and vugs are present at the same time, the vugs no longer affect the dissolution structure, but the fractures control the direction of the wormhole. Therefore, the effect of vugs can be ignored in the acidizing simulation to optimize the construction. This simplifies the calculation without affecting the result.
4) The size of vugs does not have a notable impact on the propagation of wormholes. Whether the vug is large or small, the wormhole selectively passes through a portion of the vug.
5) Under linear flow conditions, the density, orientation, and length of the fracture are key parameters for the growth direction of the wormhole. As the values of these parameters increase, their dominant effect on the wormhole direction also increases. Under radial flow conditions, the growth direction of the wormhole depends on the direction of the radius, independent of the density, length, and orientation of the fracture.

It should be noted that all the simulation results presented in the current work are for Newtonian acids. However, non-Newtonian acids are also commonly used in carbonate acidization treatment. For example, if the reservoir temperature is high, polymer-based gelled acids are normally used to retard the acid reaction rate (Maheshwari et al., 2016). For fracture-vuggy carbonate reservoirs, the formation temperature is usually high because of the deep burial of oil, and the heterogeneity is strong due to the presence of fractures and vugs. Therefore, modeling and simulation of the acidizing process with non-Newtonian acids in fractured-vuggy carbonate are necessary. This will be the focus of our future work.

Acknowledgements

The authors gratefully acknowledge the support from the National Natural Science Foundation of China (Nos. 52274057 and 51804325), the Science and Technology Support Plan for Youth Innovation of University in Shandong Province under No. 2019KJH002, 111 Project under No. B08028. The authors also gratefully acknowledge the support from King Abdullah University of Science and Technology (KAUST) through the Nos. BAS/1/1351-01, URF/1/4074-01, URF/1/3769-01.

Conflict of interest

The authors declare no competing interest.

References

Alarji, H., Clark, S., Regenauer-Lieb, K. Wormholes effect in carbonate acid enhanced oil recovery methods. Advances in Geo-Energy Research, 2022, 6(6): 492-501.

Ali, M., Ziauddin, M. Carbonate acidizing: A mechanistic model for wormhole growth in linear and radial flow. Journal of Petroleum Science and Engineering, 2020, 186: 106776.

Aljawad, M. S., Aboluhom, H., Schwalbert, M. P., et al. Temperature impact on linear and radial wormhole propagation in limestone, dolomite, and mixed mineralogy. Journal of Natural Gas Science and Engineering, 2021, 93: 104031.

Aljawad, M. S., Aljulaih, H., Mahmoud, M., et al. Integration of field, laboratory, and modeling aspects of acid fracturing: A comprehensive review. Journal of Petroleum Science and Engineering, 2019, 181: 106158.

Budek, A., Szymczak, P. Network models of dissolution of porous media. Physical Review E, 2012, 86(5): 056318.

Chen, Y., Ma, G., Li, T., et al. Simulation of wormhole propagation in fractured carbonate rocks with unified pipe-network method. Computers and Geotechnics, 2018, 98: 58-68.

Daccord, G., Lenormand, R., Liétard, O. Chemical dissolution of a porous medium by a reactive fluid—I. Model for the "wormholing" phenomenon. Chemical Engineering Science, 1993, 48(1): 169-178.

dos Santos Lucas, C. R., Neyra, J. R., Araújo, E. A., et al. Carbonate acidizing-A review on influencing parameters of wormholes formation. Journal of Petroleum Science and Engineering, 2023, 220: 111168.

Fredd, C. N., Fogler, H. S. Influence of transport and reaction on wormhole formation in porous media. AIChE Journal, 1998, 44(9): 1933-1949.

Fredd, C. N., Fogler, H. S. Optimum conditions for wormhole formation in carbonate porous media: Influence of transport and reaction. SPE Journal, 1999, 4(3): 196-205.

Furui, K., Abe, T., Watanabe, T., et al. Phase-field modeling of wormhole formation and growth in carbonate matrix acidizing. Journal of Petroleum Science and Engineering, 2022, 209: 109866.

Furui, K., Burton, R. C., Burkhead, D. W., et al. A comprehensive model of high-rate matrix-acid stimulation for long horizontal wells in carbonate reservoirs: Part I-scaling up core-level acid wormholing to field treatments. SPE Journal, 2012, 17(1): 271-279.

Golfier, F., Zarcone, C., Bazin, B., et al. On the ability of a Darcy-scale model to capture wormhole formation during the dissolution of a porous medium. Journal of Fluid Mechanics, 2002, 457: 213-254.

Hoefner, M., Fogler, H. S. Pore evolution and channel formation during flow and reaction in porous media. AIChE Journal, 1988, 34(1): 45-54.

Huang, Z., Xing, H., Zhou, X., et al. Numerical study of vug effects on acid-rock reactive flow in carbonate reservoirs. Advances in Geo-Energy Research, 2020, 4(4): 448-459.

Izgec, O., Zhu, D., Hill, A. D. Numerical and experimental investigation of acid wormholing during acidization of vuggy carbonate rocks. Journal of Petroleum Science and Engineering, 2010, 74(1-2): 51-66.

Jia, C., Huang, Z., Sepehrnoori, K., et al. Modification of two-scale continuum model and numerical studies for carbonate matrix acidizing. Journal of Petroleum Science and Engineering, 2021a, 197: 107972.

Jia, C., Sepehrnoori, K., Zhang, H., et al. Numerical studies and analyses on the acidizing process in vug carbonate rocks. Frontiers in Earth Science, 2021b, 9: 712566.

Kalia, N., Balakotaiah, V. Modeling and analysis of wormhole formation in reactive dissolution of carbonate rocks. Chemical Engineering Science, 2007, 62(4): 919-928.

Kalia, N., Balakotaiah, V. Effect of medium heterogeneities on reactive dissolution of carbonates. Chemical Engineering Science, 2009, 64(2): 376-390.

Kalia, N., Balakotaiah, V. Wormholing in perforated completions. Paper SPE 127347 Presented at the SPE International Symposium and Exhibition on Formation Damage Control, Lafayette, USA, 10-12 February, 2010.

Kardooni, M. M., Jamshidi, S. Calculating wormhole propagation and skin factor in carbonate reservoirs during directional wells acidizing. Journal of Petroleum Research, 2022, 32: 64-80.

Khoei, A. R., Sichani, A. S., Hosseini, N. Modeling of reactive acid transport in fractured porous media with the Extended-FEM based on Darcy-Brinkman-Forchheimer framework. Computers and Geotechnics, 2020, 128:

103778.

Kiani, S., Jafari, S., Apourvari, S. N., et al. Simulation study of wormhole formation and propagation during matrix acidizing of carbonate reservoirs using a novel in-situ generated hydrochloric acid. Advances in Geo-Energy Research, 2021, 5(1): 64-74.

Li, Y., Deng, Q., Zhao, J., et al. Simulation and analysis of matrix stimulation by diverting acid system considering temperature field. Journal of Petroleum Science and Engineering, 2018, 170: 932-944.

Li, Y., Liao, Y., Zhao, J., et al. Simulation and analysis of wormhole formation in carbonate rocks considering heat transmission process. Journal of Natural Gas Science and Engineering, 2017, 42: 120-132.

Liang, Y. D., Barsky, B. A. A new concept and method for line clipping. ACM Transactions on Graphics (TOG), 1984, 3(1): 1-22.

Liu, L., Huang, Z., Yao, J., et al. An efficient hybrid model for 3D complex fractured vuggy reservoir simulation. SPE Journal, 2020, 25(2): 907-924.

Liu, P., Yan, X., Yao, J., et al. Modeling and analysis of the acidizing process in carbonate rocks using a two-phase thermal-hydrologic-chemical coupled model. Chemical Engineering Science, 2019, 207: 215-234.

Liu, P., Yao, J., Couples, G. D., et al. Numerical modelling and analysis of reactive flow and wormhole formation in fractured carbonate rocks. Chemical Engineering Science, 2017a, 172: 143-157.

Liu, P., Yao, J., Couples, G. D., et al. Modelling and simulation of wormhole formation during acidization of fractured carbonate rocks. Journal of Petroleum Science and Engineering, 2017b, 154: 284-301.

Liu, M., Zhang, S., Mou, J. Effect of normally distributed porosities on dissolution pattern in carbonate acidizing. Journal of Petroleum Science and Engineering, 2012, 94: 28-39.

Liu, M., Zhang, S., Mou, J., et al. Wormhole propagation behavior under reservoir condition in carbonate acidizing. Transport in Porous Media, 2013, 96: 203-220.

Lohrasb, S., Junin, R. Pore volumes to breakthrough estimation in carbonate acidizing with hydrochloric acid by using an analytical derivation method. Petroleum, 2020, 6(4): 362-367.

Maheshwari, P., Balakotaiah, V. Comparison of carbonate HCl acidizing experiments with 3D simulations. SPE Production & Operations, 2013, 28(4): 402-413.

Maheshwari, P., Maxey, J., Balakotaiah, V. Reactive-dissolution modeling and experimental comparison of wormhole formation in carbonates with gelled and emulsified acids. SPE Production & Operations, 2016, 31(2): 103-119.

Panga, M. K., Ziauddin, M., Balakotaiah, V. Two-scale continuum model for simulation of wormholes in carbonate acidization. AIChE Journal, 2005, 51(12): 3231-3248.

Qi, N., Chen, G., Liang, C., et al. Numerical simulation and analysis of the influence of fracture geometry on wormhole propagation in carbonate reservoirs. Chemical Engineering Science, 2019, 198: 124-143.

Rafiei, Y., Motie, M. Improved reservoir characterization by employing hydraulic flow unit classification in one of Iranian carbonate reservoirs. Advances in Geo-Energy Research, 2019, 3(3): 277-286.

Ratnakar, R. R., Kalia, N., Balakotaiah, V. Carbonate matrix acidizing with gelled acids: An experiment-based modeling study. Paper SPE 154936 Presented at the SPE International Production and Operations Conference & Exhibition, Doha, Qatar, 14-16 May, 2012.

Safari, R., Smith, C., Fragachan, F. Improved recovery of carbonate reservoir by optimizing acidizing strategy; coupled wellbore, reservoir, and geomechanical analysis. Paper SPE 188683 Presented at the Abu Dhabi International Petroleum Exhibition & Conference, Abu Dhabi, UAE, 13-16 November, 2017.

Schwalbert, M. P., Zhu, D., Hill, A. D. Anisotropic-wormhole-network generation in carbonate acidizing and wormhole-model analysis through averaged-continuum simulations. SPE Production & Operations, 2019, 34(1): 90-108.

Seagraves, A. N., Smart, M. E., Ziauddin, M. E. Fundamental wormhole characteristics in acid stimulation of perforated carbonates. Paper SPE 189506 Presented at the SPE International Conference and Exhibition on Formation Damage Control, Lafayette, Louisiana, USA, 7-9 February, 2018.

Tansey, J., Balhoff, M. T. Pore network modeling of reactive transport and dissolution in porous media. Transport in Porous Media, 2016, 113: 303-327.

Wang, L., Mou, J., Mo, S., et al. Modeling matrix acidizing in naturally fractured carbonate reservoirs. Journal of Petroleum Science Engineering, 2020, 186: 106685.

Yao, J., Huang, Z. Q. Fractured Vuggy Carbonate Reservoir Simulation. Berlin, German, Springer, 2017.

Yoo, H., Nguyen, T., Lee, J. Improved wormhole prediction model considering propagation characteristics of wormhole head in carbonate acidizing. Journal of Petroleum Science and Engineering, 2022, 216: 110807.

Yoon, H., Kang, Q., Valocchi, A. J. Lattice Boltzmann-based approaches for pore-scale reactive transport. Reviews in Mineralogy and Geochemistry, 2015, 80(1): 393-431.

Yuan, T., Wei, C., Zhang, C. S., et al. A numerical simulator for modeling the coupling processes of subsurface fluid flow and reactive transport processes in fractured carbonate rocks. Water, 2019, 11(10): 1957.